Chapter 2
The LHC and ATLAS Detector

2.1 Introduction

To probe physics at the TeV scale high energy particle collisions are required. Accelerating particles to these very high energies necessitates large scale projects such as the LHC. The LHC and its four main detectors, ATLAS, CMS, LHCb and ALICE are based at CERN (the European Organisation for Nuclear Research), located on the Franco-Swiss border outside Geneva, see Fig. 2.5b. This Chapter will give a short introduction to hadron colliders, a brief description of the LHC and the CERN accelerator complex and an overview of the ATLAS detector.

The author's contribution in this Chapter is described in Sect. 2.7.2; the implementation of a framework to read information about the ATLAS semiconductor tracker configuration and display it in graphical format on a dedicated webpage.

2.2 Hadron Colliders

Since the late 1960s the experimental setup of particle colliders has remained essentially unchanged [1]. Two beams of particles (or antiparticles) accelerated and directed by electric and magnetic fields are brought together for head-on collisions at the *interaction points* inside the detectors. The collision centre-of-mass (CoM) frame approximately coincides with the laboratory frame.

The benefit of colliding beams over the preceding fixed target approach is that all the energy of the beams can be converted into mass for new particles. In fixed target experiments conservation of momentum requires that some of the collision energy must go into giving kinetic energy to the particles produced in the collision. This energy is then not available to contribute to production of heavier particles.

Although the LHC is capable of colliding ions, such as lead, the data used in this thesis are only those collected during *pp* collisions.
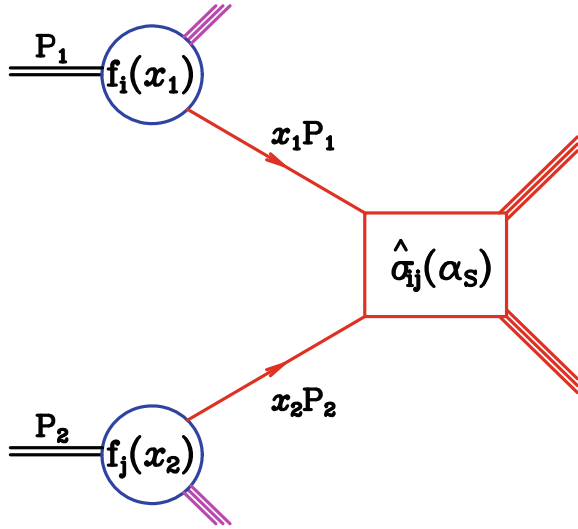
2.2.1 The Parton Model

At the high energies and correspondingly small distance scales probed at the LHC the incoming protons cannot be thought of as point particles, instead collisions are the result of interactions between quarks and gluons. The formulation for describing these interactions is known as *the parton model* [3] and is described schematically in Fig. 2.1.

In the case of an e^+e^- collider the CoM frame is the laboratory frame, however this is not the case for a pp collider. The proton constituents, u-quarks, d-quarks and gluons as well as *sea* quarks and anti-quarks that arise due to quantum fluctuations can all take part in the interaction, albeit the latter with a significantly lower probability. These partons carry some fraction, x, of the proton energy. *Deep Inelastic Scattering* (DIS) experimental measurements have shown that quarks carry only approximately 50 % of the proton energy at Q^2 100 GeV^2, the rest is carried by the gluons [4]. *Parton Distribution Functions* (PDFs) which describe the probability of a given parton having a particular x value are shown in Fig. 2.2.

As the partons involved in the hard interaction can carry different fractions of the proton momenta it is possible for there to be an asymmetry in the collision and hence the CoM frame undergoes a Lorentz boost in the z-direction. This has an important effect on event kinematics and reconstruction, introducing an additional unknown into calculations, as is discussed further in Chap. 3.
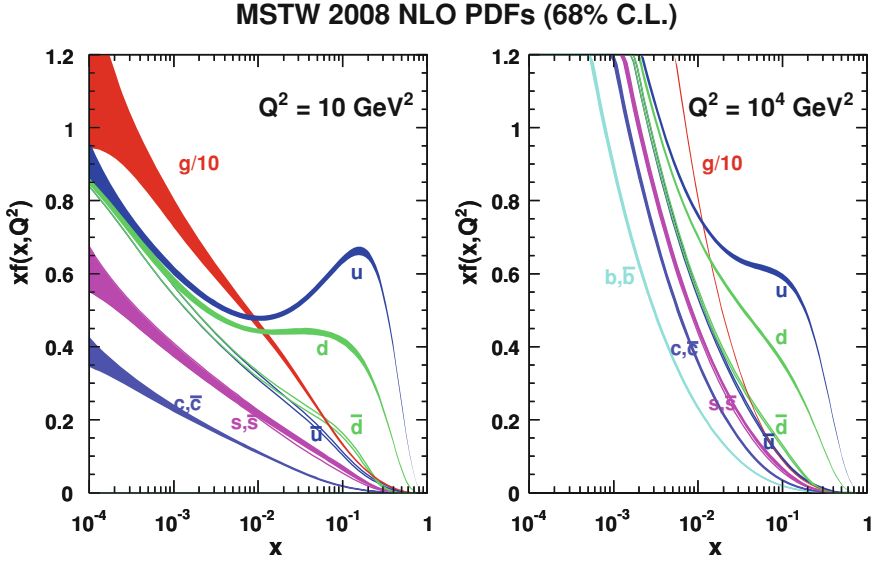
MSTW 2008 NLO PDFs (68% C.L.)

Fig. 2.2 MSTW 2008 NLO parton distribution functions at $10\,\text{GeV}^2$ (*Left*) and $10^4\,\text{GeV}^2$ (*Right*). Figures from [5]

2.2.2 Luminosity

An important consideration for any collider experiment is the number of events that will be produced for a given process. This number is given by the process production cross section multiplied by the integrated luminosity, L,

$$N_{\text{event}} = \sigma_{\text{event}} L = \sigma_{\text{event}} \int \mathcal{L}\, dt. \qquad (2.1)$$

The cross sections for a number of SM processes are shown in Fig. 2.3. The instantaneous luminosity, $\mathcal{L}$, of a pp collider is given by

$$\mathcal{L} = \frac{N_b^2 n_b f_{\text{rev}} \gamma_r}{4\pi \epsilon_n \beta^*} F, \qquad (2.2)$$

where N_b is the number of particles per bunch, n_b is the number of bunches per beam, f_{rev} is the revolution frequency, γ_r is the relativistic gamma factor, ϵ_n is the normalised transverse beam emittance, β^* is the beta function at the collision point and F is the geometric luminosity reduction factor due to the crossing angle at the interaction point [6]. The product of ϵ_n and β^* essentially gives the area of the beam spot at the interation point.

To maximise the number of events produced for a given process in a given time, it is clearly important to have the largest possible instantaneous luminosity. From (2.2)
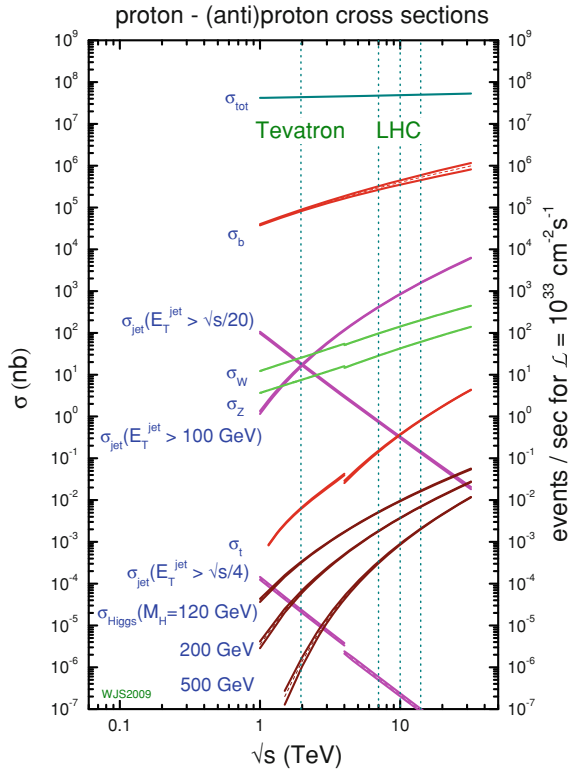
it can be seen that there are a number of ways to increase this value. For example, increasing the number of particles in the bunches or the number bunches per beam, or both.

2.2.3 Structure of an Event

Collision conditions are sensitive to the beam parameters. With an increase in the number of particles per bunch the probability of a hard collision increases, but also the number of soft interactions per bunch crossing. A single bunch crossing containing several *pp* interactions is referred to as *in-time pileup*. This can lead to a large background of predominately soft hadronic activity in collisions, which has several effects on event reconstruction, as will be described in Sect.2.5.

Increasing the number of bunches per beam can lead to more *out-of-time pileup*. This is where the detector hardware, that has an operation cycle of similar or longer timescale to the time between bunch crossings, can be affected by the bunch crossings before or after the one under consideration. However, In 2011 and 2012 data-taking
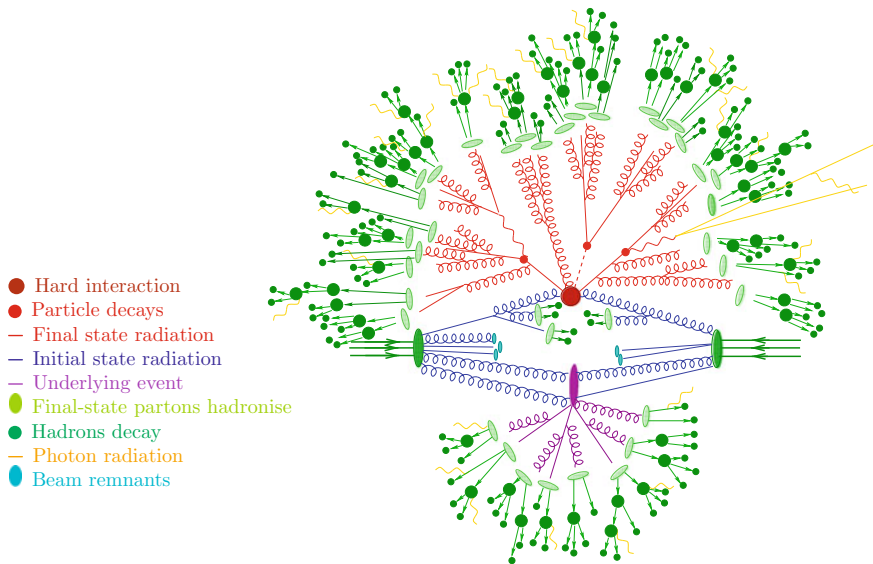
Hard interaction
Particle decays
— **Final state radiation**
— **Initial state radiation**
— **Underlying event**
Final-state partons hadronise
Hadrons decay
— **Photon radiation**
Beam remnants

Fig. 2.4 Pictorial representation of a $t\bar{t}h$ event as produced by an event generator. Figure from [7]

it has proved to be considerably less significant than in-time pileup. In the rest of this thesis, unless explicitly stated, the term pileup will relate to in-time pileup.

Another background in pp collisions comes from interactions between the remnant partons of the colliding protons not involved in the hard processes. This is referred to as the *underlying event* (UE). It is also possible to have collisions where multiple partons from the same proton are involved in hard interactions. This is referred to as *multi-parton interactions* (MPI).

Accelerated charges (colour or electromagnetic) will emit radiation. This gives rise to two other important phenomena at colliders: *initial state radiation* (ISR) and *final state radiation* (FSR). ISR corresponds to emissions associated with the incoming partons and FSR corresponds to emissions associated with the outgoing partons and decay products of particles produced in the interaction.

It is clear that the environment of a pp collision can be very messy indeed. Figure 2.4 provides a schematic diagram of the many contributions that constitute an event. A more detailed discussion of the simulation of these contributions is given in Sect. 3.5.

2.3 The Large Hadron Collider

The LHC is a particle accelerator, 27 km in circumference, capable of accelerating protons and lead ions to higher energies than any other existing experiment. Particles are accelerated around the LHC ring directed by its 1,232 dipole and 506 quadrupole superconducting magnets which operate with a peak magnetic field of 8 T.

The LHC is the final step in a chain of accelerators at CERN, see Fig. 2.5a. A humble gas bottle supplies hydrogen atoms from which the electrons are stripped using an electric field. The remaining protons are accelerated to an energy of 50 MeV by Linac 2, before being accelerated further to 1.4 GeV by the Proton Synchrotron Booster (PSB). The proton beam then enters the Proton Synchrotron (PS) and the beam energy is increased to 25 GeV. Finally, the beam is accelerated up to an energy of 450 GeV by the Super Proton Synchrotron (SPS). From here the beam is split in two and each part is accelerated around the LHC in different directions.

The two beams are forced to collide at four interaction points around the LHC. These correspond to the four main experiments ALICE, ATLAS, CMS and LHCb. The nominal design values of selected LHC operating parameters are shown in Table 2.1, along with the actual values reached during 2011 and 2012 data taking.

2.4 The ATLAS Detector

ATLAS [11] is one of four main detectors situated along the LHC ring. It is a multipurpose detector designed with the aim of operating a wide physics program, from high precision measurements to searches for new physics.

ATLAS has a mass of ∼7000 tonnes and its design is largely dominated by the choice of magnet system: a thin central superconducting solenoid and three large outer superconducting toroids. The detector consists of several different sub-detectors arranged in concentric forward-backward symmetric cylindrical layers, giving near-hermetic coverage. The inner detector, located within the solenoid and immersed in a 2 T magnetic field, is dedicated to measuring particle tracks. Starting from the detector closest to the beam pipe it is subdivided into a silicon pixel detector, a silicon strip detector, known as the semiconductor tracker (SCT), and a straw-tube tracking detector, known as the transition radiation tracker (TRT). Outside of the solenoid, the calorimetery is located. The inner electromagnetic calorimeter makes use of a liquid argon scintillator (LAr) and the outer hadronic calorimeter is constructed of iron/scintillator tiles. A toroidal magnet system is located outside of the calorimeters and is surrounded by an array of muon detectors.

2.5 Co-ordinate System

In ATLAS a combination of both cartesian and spherical co-ordinate systems are used. In both cases the origin is defined to be the nominal interaction point. In the right-handed cartesian co-ordinate system the z-axis is defined to be the direction of the beam, the positive x-axis points from the interaction point to the centre of the LHC ring and the positive y-axis points upwards. The azimuthal angle ϕ is measured around the beam axis, and the polar angle θ is the angle from the beam axis.
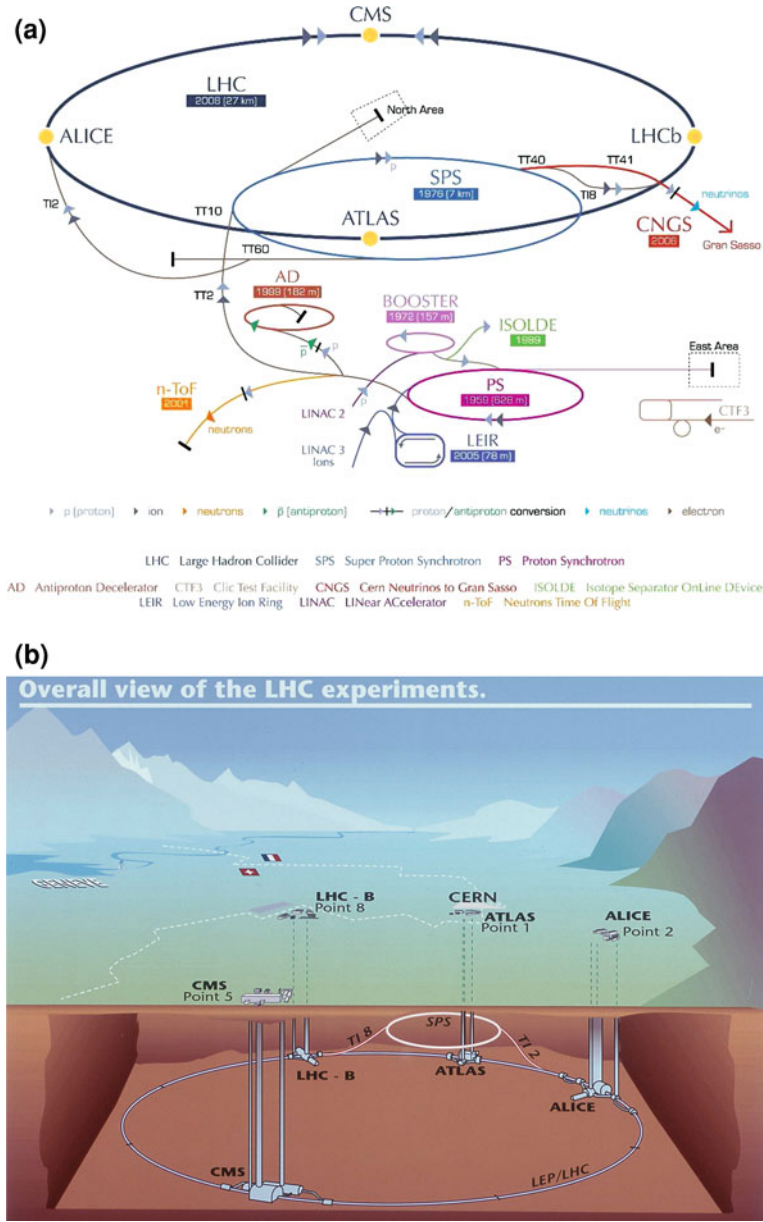
Fig. 2.5 The CERN accelerator complex (**a**) and schematic diagram of the position of the LHC and experiments underground (**b**). Figures from [8] and [9]

Table 2.1 LHC operating parameters, nominal values from LHC Design Report [6], 2011 values from 3rd Evian Workshop on LHC beam operation [10] and 2012 values from 4th Evian Workshop on LHC beam operation

Parameter	Nominal	2011	2012	Units
Proton energy	7000	3500	4000	GeV
Number of particles per bunch	1.15×10^{11}	1.45×10^{11}	1.5×10^{11}	
Number of bunches	2808	1380	1380	
Peak luminosity in IP1 and IP5	1.0×10^{34}	3.8×10^{33}	7.7×10^{33}	$cm^{-2}\ s^{-1}$
Time between collisions	49.90	49.90	24.05	ns
Delivered integrated luminosity	–	5.5	23.3	fb^{-1}

It is often useful to define variables transverse to the direction of the beam. The partons involved in hard interactions have an unknown fraction of the momentum of the incoming protons. Therefore, collisions will not be at rest in the z-direction in laboratory frame. However, in the transverse plane there is negligible net momentum, so conservation of momentum can be applied. Transverse quantities refer to projections in the x-y plane, for example transverse momentum, p_T, and transverse energy E_T. It is also useful to define the quantity pseudorapidity, $\eta = -\ln[\tan(\theta/2)]$, which is an approximation to rapidity, $y = 1/2 \ln[\frac{E+p_z}{E-p_z}]$, for massless objects. This is often used in place of θ as differences in y are invariant under longitudinal Lorentz boosts. Another useful parameter to define is the distance between objects in the η-φ plane defined as follows,

$$\Delta R = \sqrt{\Delta\varphi^2 + \Delta\eta^2}. \tag{2.3}$$

Note that this quantity is also invariant under longitudinal Lorentz boosts.

2.6 Magnet System

Precise measurement of charged particle momenta requires a strong magnetic field. ATLAS utilises a hybrid system of a central superconducting solenoid and three outer superconducting toroids. In totality the magnet system is 22 m in diameter and 26 m in length, providing a magnetic field over a volume of 12,000 m^3, with a stored energy of 1.6 GJ [11].

The solenoid provides the inner detector with a 2 T axial magnetic field. Crucially, this high field strength is obtained whilst keeping the solenoid thin in order to reduce the material in front of the electromagnetic calorimeter. The solenoid is aligned to the beam axis, it is 5.8 m in length and has an outer diameter of 2.56 m.

The toroid system is divided into three regions, the barrel and two endcaps. The barrel region is constructed from eight coils and produces a toroidal magnetic field
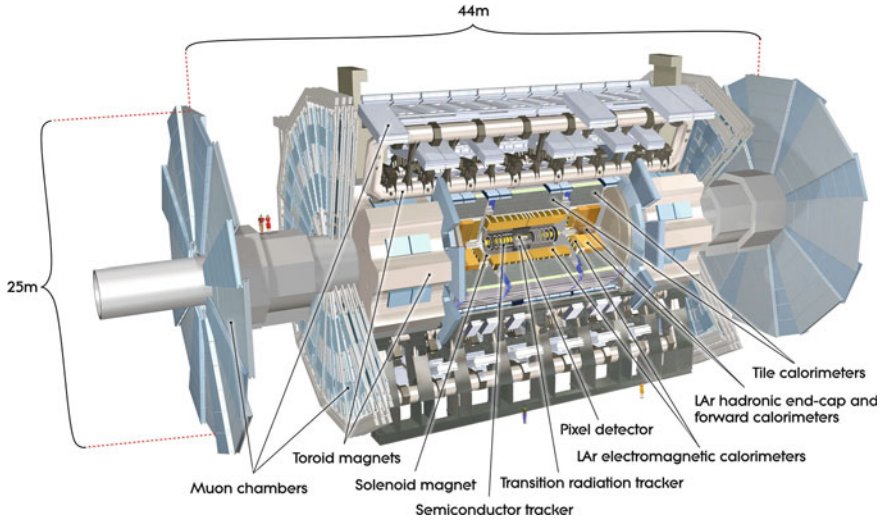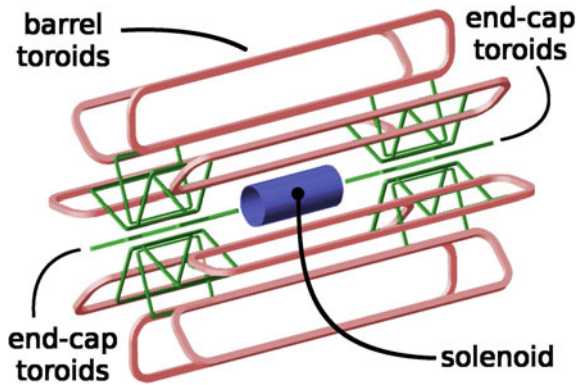
Fig. 2.6 Schematic diagram of the ATLAS detector. Figure from [11]

Fig. 2.7 Schematic diagram of the ATLAS magnet system. Figure from [12]

of approximately 0.5 T for the central muon detectors. The endcap toroids are also constructed from 8 coils each and produce a magnetic field of approximately 1 T for the muon detectors in the end-cap regions.

2.7 Inner Detector

The inner detector, shown in full in Fig. 2.8a, and with a cross section of the barrel in Fig. 2.8b, is the closest detector to the beam pipe. It is responsible for measuring the position and momentum of charged particle tracks to very high precision. This is
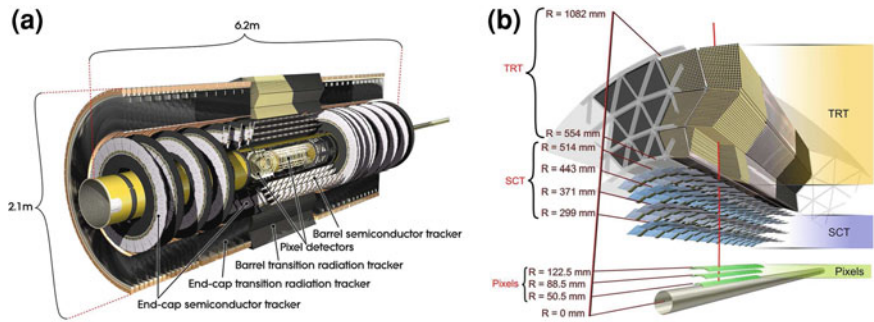
Fig. 2.8 Schematic diagram of the ATLAS inner detector (**a**) and of a particle traversing the different sub-detectors in the inner detector barrel region (**b**). Figures from [11]

Table 2.2 Inner detector intrinsic measurement accuracies [11]

Detector component	Intrinsic accuracy (μm)
Pixel	
Barrel	$10(R - \varphi)$ $115(z)$
Endcap	$10(R - \varphi)$ $115(R)$
SCT	
Barrel	$17(R - \varphi)$ $580(z)$
Endcap	$17(R - \varphi)$ $580(R)$
TRT	130

especially important for measurement of primary and secondary vertices and electron identification. With the luminosity produced by the LHC the track density in ATLAS is expected to be extremely high. In order to obtain the precise vertex and momentum resolution fine-granularity detectors are essential. The various components of the inner detector are designed to have the best possible resolution whilst minimising the amount of material placed in front of the calorimeters. The inner detector is composed of three subdetectors which are described in more detail in the following sections. Table 2.2 gives an overview of the intrinsic measurement accuracies of the inner detector subdetectors which are driven by the performance requirements of ATLAS [11].

2.7.1 Pixel Detector

The pixel detector is the closest detector the to beam line and has the finest granularity of detecting material and hence the best resolution. The pixel detector is composed of 1,744 modules each with ~50,000 $50 \times 400 \, \mu\text{m}^2$ pixels. These are arranged into 3 barrel layers and 6 endcap disks (3 on each end). In total there are ~140 million silicon pixels. The pixel detector has an intrinsic accuracy of 10 μm in the $R - \varphi$

direction and 115 μm in the z direction [11], hence its high resolution and vertexing capability.

2.7.2 Semiconductor Tracker

The semiconductor tracker (SCT) is situated outside the pixel detector and like the pixel detector is of modular silicon design. The SCT however makes use of silicon strips rather than pixels. The construction of the SCT is heavily influenced by the requirement to reduce the amount of material in front of the calorimetry which is especially important due to the relatively high density of the pixel detector.

The SCT is composed of 4,088 modules and is characterised by two regions, the barrel and endcaps. Two types of SCT module exist, one for each region. The barrel modules are arranged into 4 concentric layers (2,112 modules) and the endcaps into 18 disks, 9 on each side, (1,976 modules) [11] as shown in Fig. 2.8a. The two types of SCT modules are shown in Fig. 2.9.

Although differing in shape between barrel and endcap the general structure of all modules is the same. Each module consists of two back-to-back wafers covered with 768 silicon strips (1,536 per module). The two wafers are offset by a stereo angle of 40 mrads. This allows for 2D track hit reconstruction and reduces noise. In the barrel the SCT has a hit precision of 17 μm in the $r - \phi$ coordinate and 580 μm in the z coordinate. The forward region has a precision of 17 μm in the $z - \phi$ coordinate and 580 μm in the r coordinate [13].

2.7.2.1 SCT Readout System

The SCT modules communicate with the off-detector electronics through optical connections, as shown in the schematic diagram in Fig. 2.10a. The off-detector hardware is composed of the Data Acquisition system (DAQ) and the Detector Control Systems (DCS). The DAQ is composed of Readout Driver (ROD) crates, each containing up to 16 ROD and Back of Crate (BOC) card pairs which work together and are each responsible for 48 modules.

DCS manages the monitoring of all the detector subsystem's common infrastructure and communication with the CERN services such as cooling, power supplies, ventilation and safety. The RODs are responsible for forwarding the data on to ATLAS's Readout Buffer (ROB) which compiles all the data for event building. They also control the generation of the command signals to be sent to the BOC as well as interpreting the returning signals received by the BOC from the modules. The BOC card manages optical signals transmitted to the modules through the transmit (Tx) channels and those returning from the modules through the receive (Rx) channels. Each module has an optical package which contains one PIN[1] diode and

---

[1] $p - i - n$ junction, i stand for intrinsic silicon.

(a) 1. 4 Sensors
280 microns thick p-n
(Hamamatsu)
Strip length 12cm
Pitch 80μm
Vmax = 500V

2. 3rd Mounting point

3. Hybrid & Binary
Readout chips
Flex circuit with 12 x ABCD
chips.

7. Overlaps
Overlap in rφ and Z to
adjacent modules

8. Stereo angle
Upper or lower detector pairs
rotated by 40 mRad

4. Be Facing & Central TPG
TPG (thermal pyrolythic
graphite) plate for sensor cooling

6. Connector
Power & Data

5. Module support & Location Holes
fix to brackets, one hole & one slot

(b)

2. Hybrid & Readout chips
Flex circuit with 12 x ABCD chips.

1. 4 Sensors
280 microns thick
(Hamamatsu, CIS)
Strip length 12cm
Pitch 70-90μm
Vmax = 500V

3. Connector
Power and
redundancy

8. Mounting point
cooling interface
TPG spine for
sensor cooling

4. Opto chips
Data & Trg/Clk

7. Stereo angle
Upper or lower detector pairs
rotated by 40 mrad

6. Fanin
Detector to chip
connection

5. Hybrid support
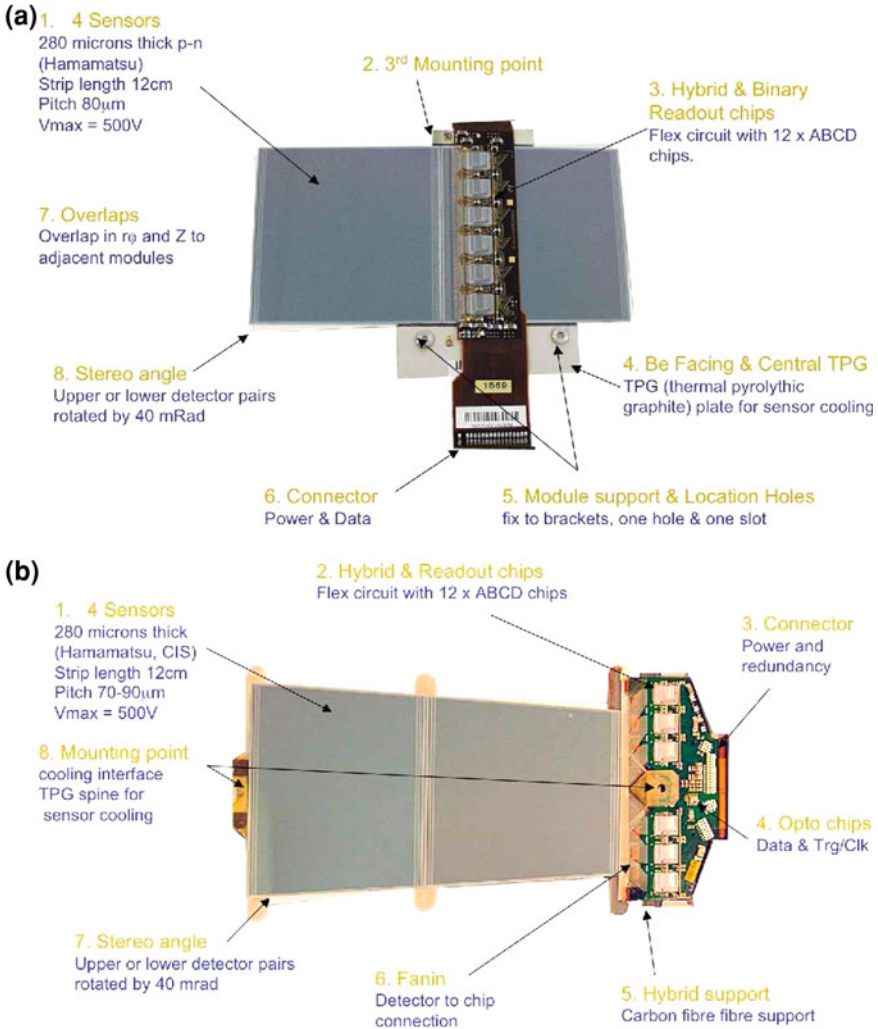Carbon fibre fibre support

Fig. 2.9 SCT barrel module (**a**) and endcap module (**b**)

two VCSELs.[2] The PIN diode receives the clock and command signals sent from the
Tx fibres and the two VCSELs send the optical signals converted from the readout
generated by the two master chips along the Rx fibres.

The module readout is initiated by a L1 accepted trigger (the ATLAS trigger
system is described in Chap. 4) signal which is sent along the Tx channel. The master
chip (as shown in Fig. 2.10b) then begins readout with a L1 trigger and bunch crossing
indicator and then reads the hit information from the chip itself before passing a token
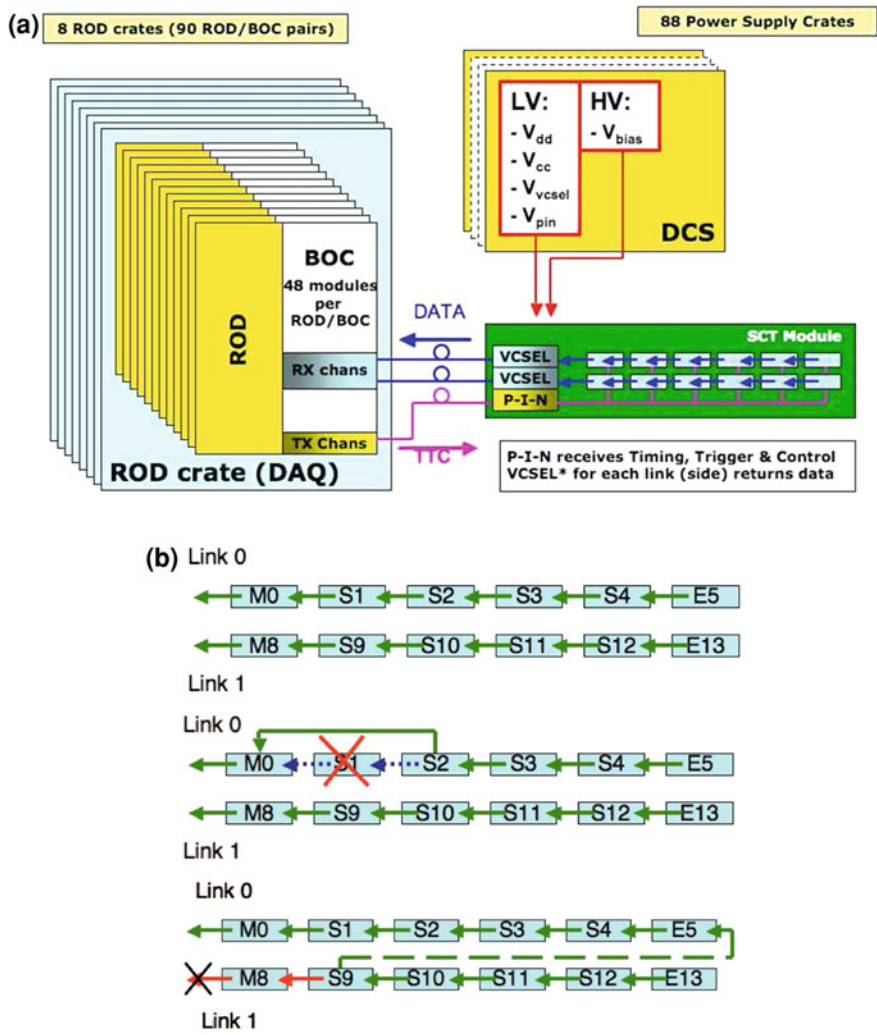
---

[2] Vertical Cavity Surface Emitting Laser.

Fig. 2.10 a SCT DAQ system schematic. **b** Standard module readout configuration (*Top*), module configuration for bypassing a failed chip (*Middle*) and module configuration for broken optical Rx link or master chip (*Bottom*). Figures from [14] and [15]

to the following chip in the chain. In the normal configuration this chain of chip data readout and token passing goes through all the chips until the end chips have read out out their hit data, see Fig. 2.10b—top. However, there are built in redundancies; if the chips or optical links fail the chain can still follow through to all other chips, examples are shown in Fig. 2.10b—middle and bottom.

Table 2.3 Module and chip parameters in configuration being monitored

Module parameter	Description
Disabled modules	Removed from data taking due to various faults
Modules in select = 0 mode	Primary (default) Tx channel is being used
Modules in select = 1 mode	Tx redundancy is being used due to issue with primary
Modules in link = 0(1) mode	Only link 0(1) Rx channel is used to read out, problem with the link 1(0) master chip or optical link
Chip parameter	Description
Masked chips	For master chips in the barrel that cannot be bypassed
Masked strips	Individual strips can be masked by the chip if they are too noisy or do not return data
Bypassed chips	Bypassed if faulty or connections between chips fail
Chip trim range settings	Chip-wide trim correction for variations in response from the front-end amplifiers for each strip
Chip thresholds	Threshold that charge deposit must exceed to record a hit

2.7.2.2 SCT Configuration Monitoring

As described above the SCT is constructed from a huge number of component parts, in total the SCT has over 6.2 million readout channels [13]. Monitoring of these parts is essential to maintain the design performance of the detector. The SCT configuration is a snapshot of the SCT settings as applied in the ATLAS control room at Point 1. Information is stored regarding each SCT strip, chip, module, ROD, BOC etc. in the configuration database.

The parameters that are monitored can be separated into two categories, those relating to SCT modules and those relating to SCT chips. For each the relevant parameters with a description of their relevance are given in Table 2.3. A selection of three of the most interesting monitored parameters plotted as function of time are shown in Fig. 2.11. The capability to display these paramters as a function of time is a unique addition to the SCT monitoring package and this is the first instance of such variables being presented in this format. The figure showing the number of modules in "select 1" mode as a function of time is of particular interest. An issue regarding the lifetime of the VCSEL packages on the BOCs was observed and confirmed by this monitoring package from the upward trend starting in May 2010. This is due to the module PINs receiving very low currents along the Tx optical fibres. Without replacements this would certainly result in large portions of the SCT being excluded from data taking. Knowing the rate of these failures and the number of replacements required is exactly the kind of information that a monitoring tool is designed to provide and neatly demonstrates the justification for such an infrastructure.
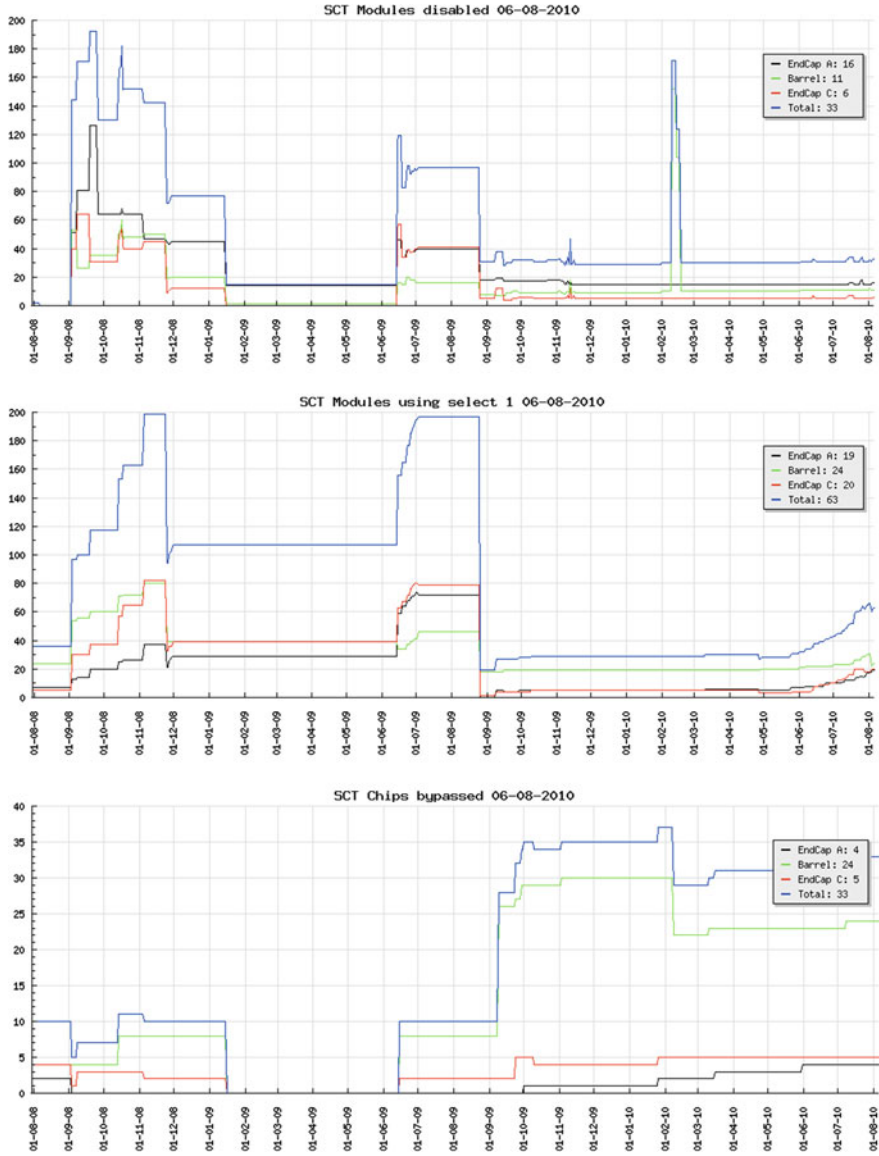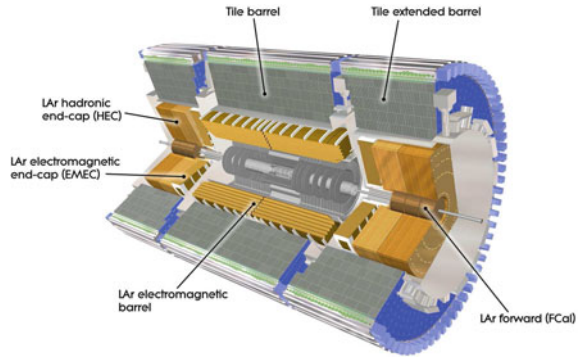
Fig. 2.11 A selection of the most interesting monitored parameters displayed as a function of time. *Top* Disabled SCT modules. *Middle* Modules using Tx redundancy. *Bottom* Total number of bypassed chips

Fig. 2.12 Schematic diagram
of the ATLAS calorimeter
system. Figure from [11]

2.7.3 TRT Detector

The TRT is the outermost layer of the inner detector. It is very different in design to
the two previously described sub-detectors and enables stand-alone electron identi-
fication. It is composed of 73 barrel layers and 224 endcap layers (112 in each) and
in total contains ~372,000 straws [16]. The straws are orientated axially in the barrel
and radially in the endcaps. Therefore the TRT gives better z resolution but worse
$R - \phi$ resolution compared to the pixel detector and SCT.

The TRT uses gas straw tubes where a charged particle passing through leaves
a trail of ionisation electrons but also transition radiation photons produced when
charged ultra-relativistic particles pass through boundaries between different media.
The energy deposit due to transition radiation photon absorption provides a charac-
teristic from which it is possible to differentiate between electrons and pions. The
time taken for the electrons to drift to the centre wire gives the distance from the
wire and hence the position and orientation of the track.

2.8 Calorimeters

The ATLAS calorimetry, located outside the inner detector, is composed of elec-
tromagnetic (EM) and hadronic sampling calorimeter systems. Two different active
media are employed; liquid argon scintillator (LAr) and plastic scintillator tiles.
The EM barrel and all endcap calorimeters (EM, hadronic and forward) make use
of the liquid argon scintillator whilst the hadronic barrel calorimeter uses a tile
scintillator. These two technologies are described in more detail in the following
Sects. 2.8.1 and 2.8.2.

The geometry of the different subcomponents of the calorimeter system can been
seen in Fig. 2.12. The EM barrel covers the range $|\eta| < 1.52$, the central barrel and
extended barrel tile calorimeters have coverage $|\eta| < 1.7$. The endcap region consists
of three sub-components; the EM endcap which has coverage $1.375 < |\eta| < 3.2$,
the LAr hadronic endcap (HEC) with coverage $1.5 < |\eta| < 3.2$ and the LAr forward

Table 2.4 Granularity of the calorimeter subdetectors [11]

Detector component	Granularity $\Delta\eta \times \Delta\phi$
EM calorimeter	
Barrel	$0.025/8 - 0.075 \times 0.025$
Endcap	$0.025/8 - 0.1 \times 0.025 - 0.1$
LAr hadronic endcap	$0.1 - 0.2 \times 0.1 - 0.2$
LAr hadronic endcap	$0.1 - 0.2 \times 0.1 - 0.2$
FCal	$3.0 - 5.4 \times 2.6 - 4.7$
Scintillator tile	
Barrel	$0.1 - 0.2 \times 0.1$
Endcap	$0.1 - 0.2 \times 0.1$

calorimeter (FCal) which covers the range $3.1 < |\eta| < 4.9$. This gives near-hermetic hadronic calorimetry coverage which is essential for accurate reconstruction of forward jets and for calculation of missing transverse momentum which is important for many of the analyses described later in this thesis. The granularity of each of the subdetectors are given in Table 2.4.

2.8.1 Liquid Argon Calorimeter

Liquid-argon is used as the active detector medium in the EM barrel calorimeter and all three subdetectors in the endcaps. This allows the endcap modules to share the same cryostat.

The barrel and endcap EM calorimeters are constructed with an accordion geometry as shown for a barrel module in Fig. 2.13. In the barrel the accordion waves are axial and run in ϕ, in the end-caps the waves are radial and run axially. This allows readout of the signal from either end of the module and avoids cracks in the direction of the waves. The absorbing material in this case is lead. The hadronic endcap calorimeters are constructed with a flat-plate design and use copper plates as the absorbing material. The forward calorimeter is split into three segments; an inner EM module (FCal1) where copper is used as the absorbing material and two outer hadronic modules (FCal2 and FCal3) where tungsten is the absorbing material.

Figure 2.14a, b show the amount of material in front of and including the EM calorimeters. Significant material before the accordion modules can lead to energy losses to incident particles, therefore pre-samplers are placed before these modules in order to correct for such losses. The EM barrel provides at least 22 radiation lengths of material which ensures that all the EM shower will be contained within the calorimetry.

2.8.2 Tile Calorimeter

The tile calorimeter is segmented into three sections, the central barrel ($|\eta| < 1.0$) and two extended barrels ($0.8 < |\eta| < 1.7$). The active medium is scintillating plates
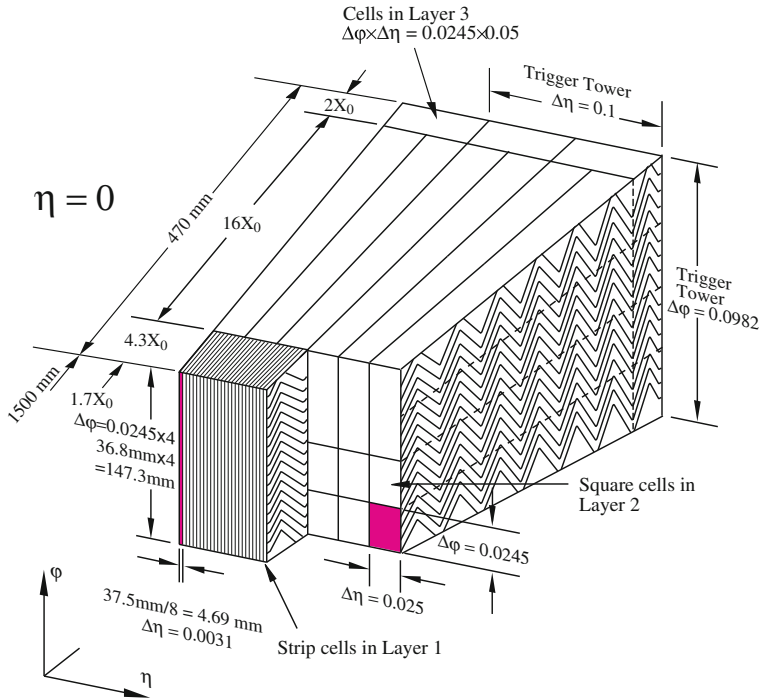
Fig. 2.13 Schematic diagram of the EM barrel calorimeter module construction. Figure from [11]

and the absorber is steel. The main purpose of the tile calorimeter is the energy reconstruction of jets and, combined with the endcap and forward calorimeters, measurement of the missing transverse momentum.

The design of a tile calorimeter module is shown in Fig. 2.15a. The steel absorbing material and scintillator active material are arranged in a periodic structure in planes perpendicular to the beam allowing for excellent coverage in ϕ.

Figure 2.15b shows the amount of material that each part of the ATLAS calorimetry contributes. Across the whole range of η the calorimetry provides at least 10 interaction lengths of material which ensures that the full hadronic shower will be contained within the calorimeter even up to very high energies.

2.8.3 Energy Resolution

For several key analyses at ATLAS excellent energy resolution is required. For example in $H \to \gamma\gamma$ searches where good mass resolution, and hence EM energy resolutions, is key to identifying a narrow resonance above the large irreducible $\gamma\gamma$ background. Also jet energy resolution is vital for many analyses, for example the measurement of the top quark mass and SUSY searches in hadronic final states.
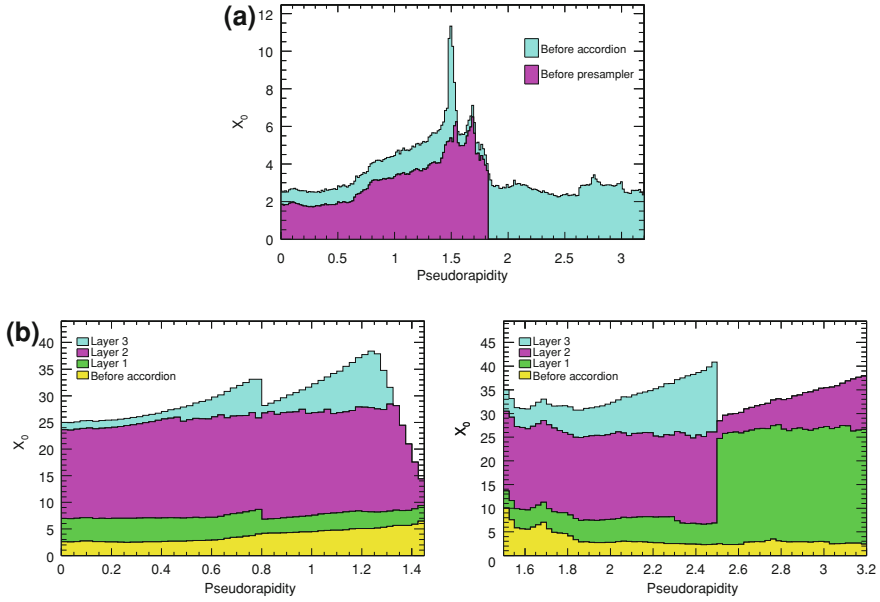
Fig. 2.14 Cumulative amount of material in front of (**a**) and including (**b**) the EM calorimeters as a function of $|\eta|$ in units of radiation length X_0. Figures from [11]

The energy resolution can be described with the following expression [17],

$$\frac{\sigma}{E} = \frac{a}{\sqrt{E}} \oplus \frac{b}{E} \oplus c \tag{2.4}$$

where a is the *s*tochastic term due to the intrinsic fluctuation in the shower evolution, b is the *noise term* due to electronic noise in the readout chain and c is the *constant term* due to instrumental effects. The LHC performance goals for energy resolution are summarised in Table 2.5.

2.9 Muon Spectrometer

The muon spectrometer is designed to measure the momentum of charged particles exiting the calorimetry system in the region $|\eta| < 2.7$ and trigger on those charged particles for $|\eta| < 2.4$. The detector is required to give standalone high precision transverse momentum resolution (10 % for 1 TeV tracks) [11]. The tracking chambers are oriented in 3 concentric cylindrical layers in the barrel and in large wheels perpendicular to the beam axis in the endcaps, see Fig. 2.16.

The precision tracking chambers in the barrel use Monitored Drift Tubes (MDTs) over most of the η range. In the forward region of the inner most layer $2 < |\eta| < 2.7$

Fig. 2.15 a Schematic diagram of a tile calorimeter module. **b** Cumulative amount of material in front of and including the calorimeter systems as a function of $|\eta|$ in units of interaction length I_0. Figures from [11]
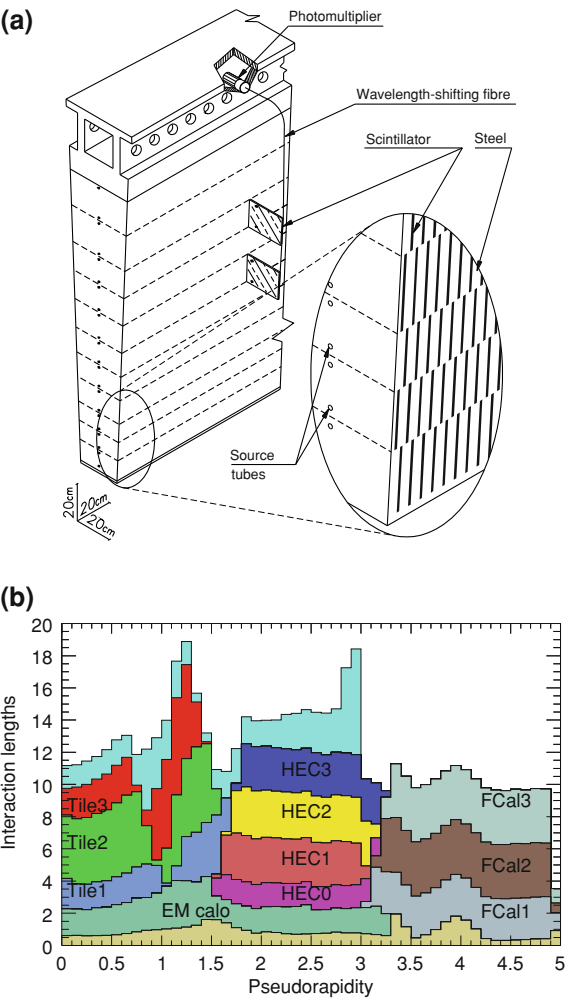

Table 2.5 Calorimeter energy resolution performance goals

Detector component	Required resolution
EM calorimetry	$\sigma/E = 10\%/\sqrt{E} \oplus 0.7\%$
Hadronic calorimetry	
Barrel	$\sigma/E = 50\%/\sqrt{E} \oplus 3\%$
Endcap	$\sigma/E = 100\%/\sqrt{E} \oplus 10\%$

Cathode Strip Chambers (CSCs) are used. In the trigger system Resistive Plate Chambers (RPCs) are used in the barrel whilst Thin Gap Chambers (TGCs) are used in the endcaps.

Fig. 2.16 Schematic diagram of the ATLAS muon spectrometer. Figure from [11]
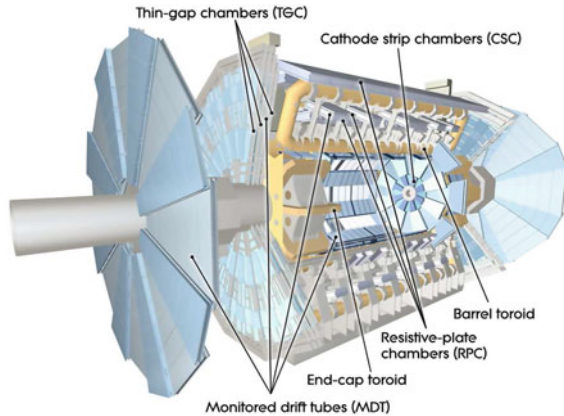
References

1. M. Perelstein, *Introduction to Collider Physics*, arXiv:1002.0274 [hep-ph]
2. R.K. Ellis, W.J. Stirling, B.R. Webber, *QCD and Collider Physics*. Cambridge monographs on particle physics, nuclear physics, and cosmology. Cambridge Univ. Press, Cambridge, 2003. Photography by S. Vascotto
3. R.P. Feynman, *Photon-hadron interactions* (Benjamin, New York, 1972)
4. R. Wallny, *A Measurement of the Gluon Distribution in the Proton and of the Strong Coupling Constant*, http://www-h1.desy.de/psfiles/theses/h1th-284.pdf
5. A. D. Martin et al., Parton distributions for the LHC. Eur. Phys. J. **C63**, 189–285 (2009) arXiv:0901.0002 [hep-ph]
6. Brüning, Oliver Sim and Collier, Paul and Lebrun, P and Myers, Stephen and Ostojic, Ranko and Poole, John and Proudlock, Paul, LHC Design Report. CERN, Geneva, 2004. https://cds.cern.ch/record/782076
7. T. Gleisberg et al., Event generation with SHERPA 1.1, JHEP **02**, 007 (2009). arXiv:0811.4622
8. C. Lefevre, The CERN accelerator complex. Complexe des acclrateurs du CERN, Dec, 2008. https://cds.cern.ch/record/1260465
9. AC Team, The four main LHC experiments (1999). https://cds.cern.ch/record/40525
10. Proceedings of the 3rd Evian Workshop on LHC beam operation. CERN, Geneva, 2011. https://cdsweb.cern.ch/record/1451243/
11. ATLAS Collaboration, The ATLAS Experiment at the CERN Large Hadron Collider, JINST **3**, S08003 (2008)
12. J. Goodson. http://www.jetgoodson.com/images/thesisImages/magnetSystems.png
13. ATLAS Collaboration, ATLAS inner detector: Technical design report. Vol. 2, CERN-LHCC-97-17
14. D. Robinson, Silicon central tracker commissioning in ATLAS, commissioning of the ATLAS silicon tracker. PoS Vertex **2007**, 001 (2007)
15. B.M. Demirkoz, T. Weidberg, Construction and performance of the ATLAS SCT barrels and cosmic tests (2007)
16. ATLAS: Detector and physics performance technical design report. Volume 1, CERN-LHCC-99-14.
17. C. Fabjan, F. Gianotti, Calorimetry for particle physics. Rev. Mod. Phys. **75**, 1243–1286 (2003)

Third generation SUSY and t̄t +Z production
Searches using the ATLAS detector at the CERN Large
Hadron Collider
McFayden, J.